Journal of
Biomedical Optics

BiomedicalOptics.SPIEDigitalLibrary.org

In vivo photoacoustic imaging of blood vessels using a homodyne interferometer with zero-crossing triggering

Jiao Lu
Yingzhe Gao
Zhenhe Ma
Hongxian Zhou
Ruikang K. Wang
Yi Wang

Jiao Lu, Yingzhe Gao, Zhenhe Ma, Hongxian Zhou, Ruikang K. Wang, Yi Wang, "*In vivo* photoacoustic imaging of blood vessels using a homodyne interferometer with zero-crossing triggering," *J. Biomed. Opt.* **22**(3), 036002 (2017), doi: 10.1117/1.JBO.22.3.036002.

Journal of Biomedical Optics 22(3), 036002 (March 2017)

In vivo photoacoustic imaging of blood vessels using a homodyne interferometer with zero-crossing triggering

Jiao Lu,[a] Yingzhe Gao,[a] Zhenhe Ma,[a] Hongxian Zhou,[a] Ruikang K. Wang,[b] and Yi Wang[a,*]
[a]Northeastern University at Qinhuangdao, School of Control Engineering, Qinhuangdao, China
[b]University of Washington, Department of Bioengineering, Seattle, Washington, United States

Abstract. We demonstrate a quasinoncontact photoacoustic imaging method using a homodyne interferometer with a long coherence length laser. The generated photoacoustic signal is detected by a system that is locked at its maximum sensitivity through the use of balanced detection and zero-crossing triggering. The balanced detector is substantially equalized, so its output is zero when the system reaches the maximum sensitivity. The synchronization approach is used to trigger the excitation and detection of the photoacoustic signal. The system is immune to ambient vibrations. A thin water layer on the sample surface is used to reduce the effect of the rough tissue surface. The performance of the system is demonstrated by *in vivo* imaging of the microvasculature in mouse ears. [DOI: 10.1117/1.JBO.22.3.036002]

Keywords: photoacoustic imaging; quasinoncontact; homodyne interferometer; zero-crossing trigger.

Paper 160814R received Nov. 30, 2016; accepted for publication Feb. 10, 2017; published online Mar. 2, 2017.

1 Introduction

Photoacoustic imaging (PAI) has evolved into a powerful tool for imaging endogenous tissue chromophores, especially the hemoglobin that plays a crucial role in maintaining normal physiological function. PAI has been widely used for imaging of various biological tissues.[1–6] In most PAI systems, an acoustic detector, such as an ultrasound transducer,[7–9] a Fabry–Perot polymer film ultrasound sensor,[10] or an optical fiber detector,[11] is used to measure the photoacoustic pressures, and physical contact between the detector and the sample is required due to the high reflection loss of ultrasonic waves at the air–tissue boundary and their rapid attenuation in air. For example, in a transducer-based PAI system, the transducer and the scanning unit are generally immersed in water, and a close contact is required between the sample and the water tank through a piece of membrane.[7,9] Although the Fabry–Perot ultrasound sensor-based system uses an optical method to measure photoacoustic waves, the sensor head is still required to be placed on the sample surface. The contact detection configuration complicates the imaging process, and the acoustic coupling level between the sample and the acoustic detector influences photoacoustic signals. Moreover, physical contact is sometimes susceptible to the alternation of physiological conditions of the object under investigation.

In recent years, various optical interferometry-based PAI methods have been proposed, such as using a homodyne interferometer, a heterodyne interferometer, a two-wave mixing interferometer, or a confocal Fabry–Perot interferometer.[12–20] These methods remotely measure the transient displacement of the sample surface caused by photoacoustic pressures and have the potential for PAI in noncontact mode. The feasibility of noncontact PAI has been demonstrated using phantoms.[12–18] However, the rough surfaces of biological tissues and random ambient vibrations could deteriorate the sensitivities of these systems. The rough tissue surface causes position-dependent issues such as laser speckles, fluctuations in the intensity of the probe light backscattered by the tissue surface, and unstable optical path length differences (OPLD) between the probe and reference arms. Attempts have also been made to image blood vessels using a low-coherence interferometer.[18–20] However, these results also showed a low sensitivity because the sensitivity of the low-coherence interferometer decreases with the increase of OPLD. Compared with the transducer-based PAI, the recently developed optical interferometry-based methods have relatively low sensitivity and cannot yet provide photoacoustic images of biological tissue with high quality.[12–20] Moreover, the probe beam that is backscattered from different depths in the tissue could result in an ambiguous depth-interpretation. Air-coupled ultrasound detection has also been demonstrated for noncontact PAI;[21] however, its sensitivity is relatively low due to the mismatch of acoustic impedance.

For an optical interferometer, the maximum sensitivity corresponds to an OPLD of $k\pi \pm \pi/2$. In our previous study, we demonstrated the feasibility of PAI using a low-coherence interferometer,[18] in which the OPLD between the probe and reference arms can be locked at $k\pi \pm \pi/2$ during imaging. The system is easily combined with OCT, which uses the same low-coherence light source. However, the sensitivity of the low-coherence interferometer decreases with the increase of the OPLD, and it turns to zero when the OPLD is greater than the coherence length of the laser source. It is difficult to stabilize such a system at a constant high sensitivity during imaging. To address this problem, we present a PAI system using a homodyne interferometer with a long coherence length laser, which allows a constant high sensitivity in a large dynamic range of the OPLD. The system can be locked at its maximum sensitivity

---

*Address all correspondence to: Yi Wang, E-mail: wangyi@neuq.edu.cn

using a synchronization approach similar to that used in our previous study.[18] A thin water layer on the sample surface is used to reduce the effect of the rough tissue surface, and we detect the vibration of the water surface caused by the photoacoustic wave emitted from the inside of the sample. The water surface provides a homogeneous surface for optical detection, with which the position-dependent effect of the tissue surface is reduced.

2 Methods and Setup

The schematic of the experimental setup is shown in Fig. 1(a). It is a homodyne fiber interferometer with balanced detection and multisynchronization. To reduce the influence of the rough tissue surface, the region for imaging was covered with a thin water layer with a thickness of several millimeters. A diode-pumped solid-state laser with a wavelength of 527 nm and a pulse duration of 7 ns was employed to excite photoacoustic waves. A distributed feedback laser diode with a wavelength of 1310 nm and a linewidth of 0.1 nm was used as the light source of the interferometer. The coherence length of the probe laser was ∼17 mm. The balanced detection configuration mainly comprised three three-port fiber circulators and a balanced photodetector (PDB410C, Thorlabs) with a bandwidth of 100 MHz. The light emitted from the probe laser source was coupled into circulator 1, and the output light was divided into the reference and probe arms by a 2×2 fiber coupler with a coupling ratio of 50/50. The probe beam and the excitation beam were combined together with a dichroic mirror and then were focused by an achromatic lens with a focal length of 50 mm. The excitation beam and the probe beam were focused in the sample and on the water surface, respectively. The distance between the two focus points was adjusted by changing the separation between lenses 1 and 2. The probe light intensity backscattered from the water surface is much greater than that backscattered from other depths, so the ambiguous depth-interpretation resulted from the probe light backscattered from multiple depths is removed.

We used a galvanometer scanner and a motor-stage to achieve fast scanning along the X-axis and slow scanning along the Y-axis, as shown in Fig. 1(b). The fast scanning configuration is shown in Fig. 1(c). The water layer covering the sample provided a natural horizontal surface, and the probe beam was adjusted along the vertical orientation. The distances between the achromatic lens and the scanning mirror and between the achromatic lens and the water surface were equal to the focal length of the achromatic lens, so the probe light intensity reflected from each scanning point on the water surface was nearly identical.

The maximum sensitivity of the homodyne interferometer corresponds to OPLDs of $k\pi \pm \pi/2$, resulting in a zero output of the balanced photodetector if the pair of photodiodes is precisely equalized. However, ambient vibrations often generate a stochastic OPLD change, which is much greater than that caused by photoacoustic waves, leading to a fluctuating sensitivity for the system. To address this problem, we used multisynchronization and balanced detection to lock the system at its maximum sensitivity. The balanced detector was precisely equalized by adjusting mirrors 1 and 2 [as shown in Fig. 1(a)]. The system reaches its maximum sensitivity when the output voltage of the balanced photodetector is zero. A voltage comparator was used to continuously detect the output signal of the balanced detector, and the excitation and detection of the photoacoustic wave were triggered when the output of the balanced photodetector was zero.

The schematic of multisynchronization is shown in Fig. 2. A representative signal detected from the water surface caused by random ambient vibrations is plotted in Fig. 2(a), where the top and bottom parts of the signal reach saturation. The vertical dotted lines show the time of emergence of zero output from the balanced detector. The voltage comparator sent a trigger signal

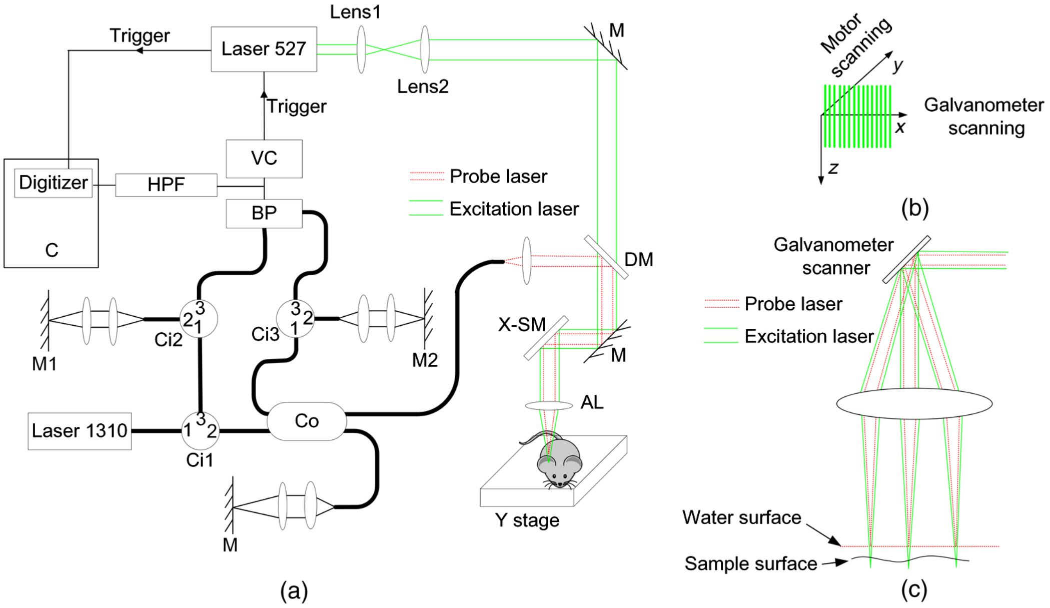

Fig. 1 (a) Schematic of the experimental setup. M, mirror; Ci, circulator; Co, coupler; BP, balanced photodetector; VC, voltage comparator; HPF, high-pass filter; C, computer; X-SM, X scanning mirror; AL, achromatic lens; DM, dichroic mirror. (b) Fast scanning along the X-axis and slow scanning along the Y-axis. (c) Galvanometer scanning configuration.

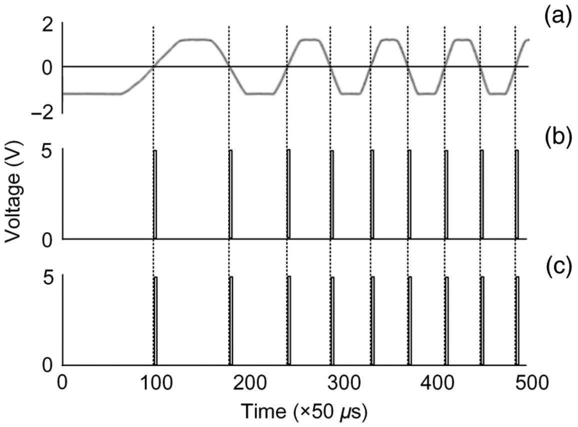

Fig. 2 Schematic of multisynchronization. (a) Representative signal detected from the water surface. The vertical dotted lines show the time of emergence of zero. (b) Trigger signals for exciting photoacoustic waves. (c) Trigger signals for detecting photoacoustic waves.

(the first trigger signal) to the excitation laser source if the output signal of the balanced detector was zero, as shown in Fig. 2(b). The excitation laser source was triggered to emit a pulsed laser for exciting the photoacoustic wave. Simultaneously, a synchronization signal (the second trigger signal) was generated by the pulsed laser to trigger a high-resolution digitizer (PCI 5124, National Instruments) for the detection of the photoacoustic signal, as shown in Fig. 2(c). The sampling frequency of the digitizer was 100 MHz. The time delay between the emergence of zero voltage and starting the detection of photoacoustic signals was less than 400 ns. Thus, the system was locked at its highest sensitivity for detecting each photoacoustic signal. A high-pass filter with a cutoff frequency of 15 kHz was used to reject residual DC voltage. It seems that the second trigger signal is not necessary because the excitation laser and the digitizer could be triggered by the first trigger signal simultaneously. Because the excitation laser source used in this study occasionally failed to emit pulsed laser light in trigger mode, we triggered the digitizer with the synchronization signal generated by the pulsed laser light to ensure the validity of each trigger signal sent to the digitizer.

3 Results and Discussion

We first imaged a black tape and the edge of a sharp blade to test the axial and lateral resolutions of the present system.[22] In Fig. 3(a), the circles show the maximum amplitude projection (MAP) data of a B-scan crossing the blade edge, and the corresponding smoothed result is displayed as the solid line. The lateral line spread function (LLSF) shown as the dashed line was obtained by calculating the first derivative of the smoothed result, and the full width at half maximum (FWHM) of the LLSF was considered the lateral resolution. The measured lateral resolution was 11 μm. An A-line photoacoustic signal of the black tape, representing the axial line spread function (ALSF), is shown in Fig. 3(b). Similarly, the FWHM of the ALSF was used to estimate the axial resolution. The measured FWHM was 25 ns, corresponding to an axial resolution of 37.5 μm (calculated with a sound speed of 1.5 mm/μs).

Next, we imaged a phantom comprising four human hairs embedded in a scattering gel to test the performance of the proposed system. The scattering gel was made of agar mixed with 1% intralipid, which gave a scattering background similar to that of highly scattering tissue. The phantom was immersed in water, and the distance between the water surface and the hairs was ~2 mm. The laser fluence was 23 mJ/cm^2. The imaging region was 1.7×3 mm^2 (230×400 pixels), and the steps along the X-direction and Y-direction were each 7.5 μm. Figure 4 shows the resulting images of the phantom. The photoacoustic MAP image and the corresponding wireframe mesh are shown in Figs. 4(a) and 4(b), respectively. The three-dimensional (3-D)-rendering image is shown in Fig. 4(c). The hairs are clearly visible with high contrast. Hairs 1 and 2 laid above hairs 3 and 4 with a distance of ~0.7 mm and shadowed hairs 3 and 4 at positions A and B, respectively. In Fig. 4(b), the amplitudes of the detected photoacoustic signals along hair 1 are nearly equal, and it is same with hair 2. The hairs have high optical absorption, and the photoacoustic signals from hairs 1 and 2 are close to saturation. The amplitudes of detected photoacoustic signals from hairs 3 and 4 have little fluctuation, indicating that the system has a constant high sensitivity for each scanning point.

We used the proposed system to image the blood vessels in a mouse ear *in vivo* to verify its capability for imaging of biological tissue. A 9-week-old mouse (female) was used in this study with the approval of the Animal Ethical Committee of Northeastern University (Shenyang, China), and all the experiments were conducted according to the National Institutes of Health Guide for the Care and Use of Laboratory Animals. The mouse was anesthetized using a mixture (ketamine, 80 mg/kg; xylazine, 6 mg/kg) through an intraperitoneal injection. During the experiment, the mouse's temperature was kept at 37°C by a heating pad. The hair on the mouse ear was gently removed to improve light penetration. The mouse ear was pasted flat onto a glass block. We used dental cement to create a closed wall around the region for imaging [Fig. 5(a)] in which a water layer was formed to eliminate the influence of the rough surfaces of the ear. The enlarged region of the dashed line box is shown in Fig. 5(b). The laser fluence incident on the skin surface was 26 mJ/cm^2, close to 20 mJ/cm^2, the Approved American National Standard for skin at this wavelength. Figures 5(c) and 5(d) show the experimental results obtained from a region of 1.5×3 mm^2 (200×400 pixels) and a region of 3×3 mm^2 (400×400 pixels), respectively, marked with two black rectangles, as shown in Fig. 5(b). The scanning steps along the X-direction and Y-direction were each 7.5 μm. The *in vivo* photoacoustic MAP images of the microvasculature in regions 1 and 2 are shown in Figs. 5(c) and 5(d), respectively. Figure 5(e) is the profile of the MAP data along the dotted line as shown in Fig. 5(c). The microvasculature can be clearly observed with high contrast, and they cannot be distinguished in the photograph of the mouse ear. The resulting images indicate that the present system is suitable for *in vivo* imaging of blood vessels with high contrast.

The closed wall created on the sample surface provides a relatively large region for imaging, but sometimes it is not convenient. For the case of imaging of a small region, such as photoacoustic microscopy, the closed wall is not necessary. *In vivo* PAI of the microvasculature in another mouse ear without creating a dental cement wall was also performed. The mouse was prepared as described above. The mouse ear was pasted flat onto a glass block. A big drop of water was spread out on the ear surface as shown in Fig. 6(a), where the box indicates the imaging region (1.5×1.5 mm^2). The *in vivo* photoacoustic MAP image (200×200 pixels) is shown in Fig. 6(b). As a contrast, the result from the same region without a water

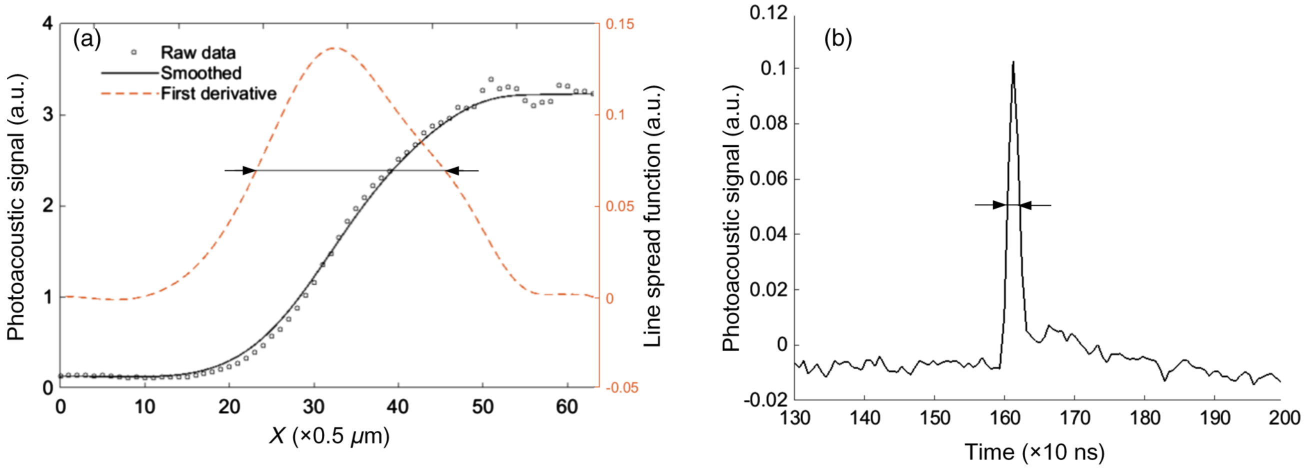

Fig. 3 Lateral and axial spatial resolutions of the present system. (a) Photoacoustic MAP data of a B-scan crossing the edge of a sharp blade. (b) Photoacoustic signal of a black tape.

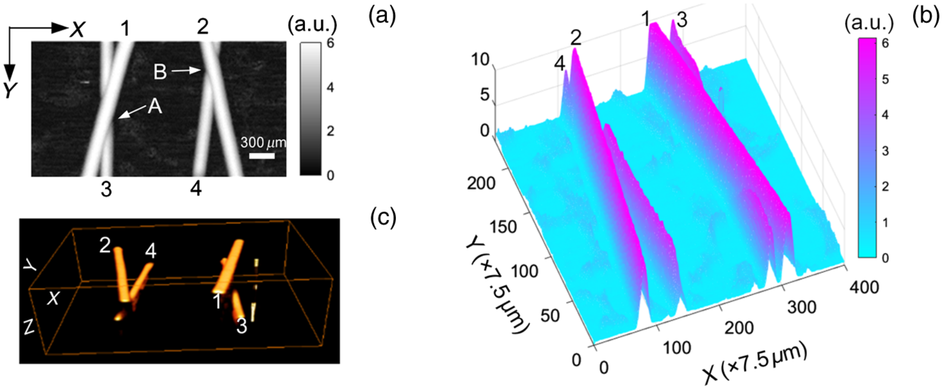

Fig. 4 Resulting images of the phantom. (a) MAP image. (b) Wireframe mesh image. (c) 3-D-rendering image. The color bar indicates photoacoustic intensity in arbitrary units.

layer is shown in Fig. 6(c). In Fig. 6(b), the microvasculature can be clearly distinguished with high contrast. However, in Fig. 6(c), only the relatively thick blood vessels can be seen with a low contrast.

The above experimental results confirm that the present method can be successfully utilized for PAI of biological tissue. Compared with the relatively complicated interferometry-based PAIs reported previously, such as using a homodyne interferometer with active stabilization, a heterodyne interferometer, a two-wave mixing interferometer, or a confocal Fabry–Perot interferometer,[12–20] the present system is based on a simple homodyne interferometer without active stabilization. During imaging, the interferometer is stabilized at its maximum sensitivity using a zero-crossing trigger method. From the results shown in Figs. 6(b) and 6(c), it can be seen that the water layer on the sample surface plays a crucial role in the optical interferometry-based PAI. Although the present method remotely measures the transient displacement of the water surface caused by photoacoustic pressures, it is not a completely noncontact mode because a water layer is still required. We call this a quasinoncontact mode. Compared with the PAI in contact mode, the present method has less influence on the sample and is more convenient for imaging of biological tissues, especially in the case in which the closed wall is not required. Moreover, the system is easily combined with other optical imaging techniques.

The axial resolution of PAI is mainly limited by the systematic bandwidth. For vibration detection with optical interferometric methods, the bandwidth is mainly dependent on the focus spot size of the probe beam and limited by the bandwidth of the photodetector (which is 100 MHz in this study). The detection bandwidth can be very high due to the relatively small beam spot size that a probe beam can be focused into. The FWHM of the pulsed photoacoustic signal shown in Fig. 3(b) is 25 ns, corresponding to an estimated bandwidth of 40 MHz (the reciprocal of the FWHM). The detection bandwidth for the present system can be improved by decreasing the focus spot size of the probe beam.

The laser fluence incident on the ear surface was 26 $\mathrm{mJ/cm^2}$, slightly greater than 20 $\mathrm{mJ/cm^2}$, the Approved American National Standard. Note that the system used in this study is not yet in the optimal configuration. The systematic sensitivity could be further improved, allowing a safe incident laser fluence. For example, averaging is a simple and efficient method of increasing the signal-to-noise ratio of a signal. The imaging results shown above were taken without averaging due to the limited imaging speed of the system. Therefore, the sensitivity can be improved if averaging is performed. For the present system, the imaging speed is mainly limited by the pulse repetition rate of the excitation laser used in this study (less than 1 KHz in trigger mode) and the zero-crossing frequency of the

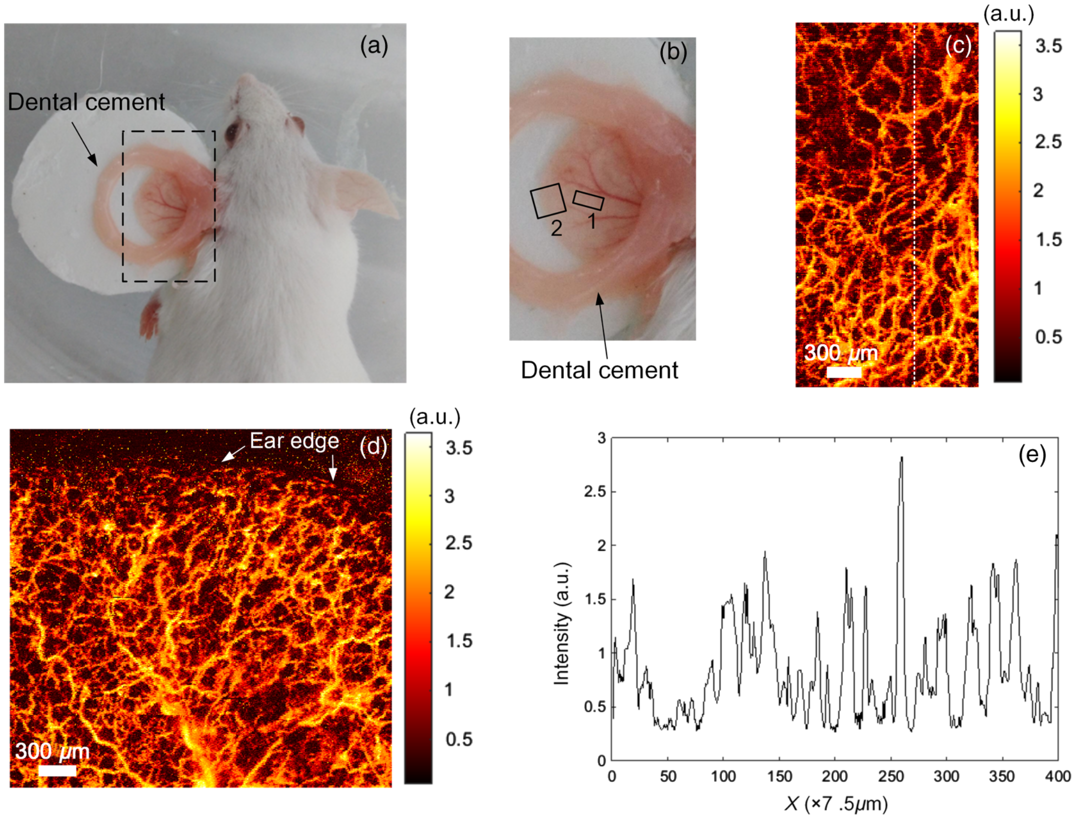

Fig. 5 (a) Photograph of a mouse ear with a closed wall made of dental cement. (b) The enlarged region of the dashed line box in (a). *In vivo* photoacoustic images of blood vessels in the mouse ear obtained from (c) region 1 and (d) region 2. (e) Profile of the blood vessels along the dotted line in (c). The color bar indicates photoacoustic intensity in arbitrary units.

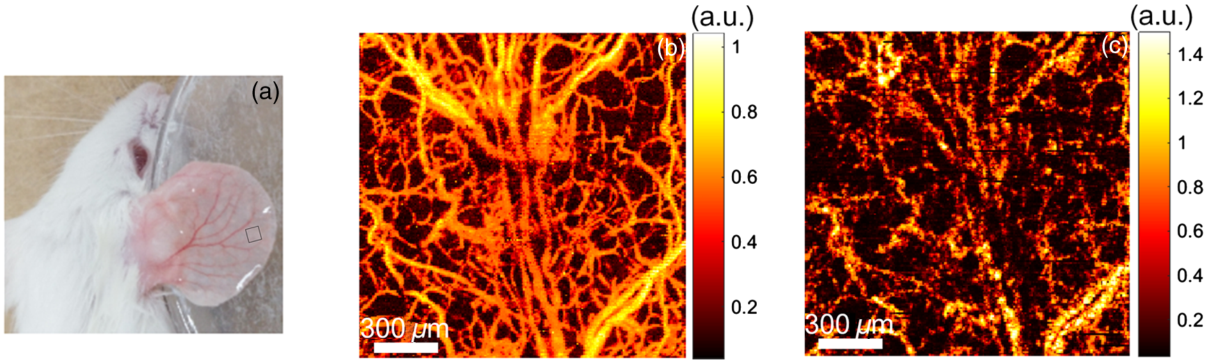

Fig. 6 (a) Photograph of a mouse ear. The box indicates the imaging region. *In vivo* photoacoustic MAP images of blood vessels in the mouse ear (b) with and (c) without a water layer. The color bar indicates photoacoustic intensity in arbitrary units.

interference signal. The total time taken to acquire an image with 400×400 pixels was ∼10 min. The zero-crossing frequency could be increased by moving the reference mirror. For example, moving the reference mirror with a speed of 10 mm/s offers a zero-crossing frequency of 30 KHz. The theoretical maximum imaging speed is dependent on the propagation time of the photoacoustic wave in the sample and water layer. Supposing that the thickness of the water layer and the detection depth in the sample are each 1 mm and the total propagation time is less than 2 μs, then the theoretical maximum imaging speed for one signal is 500 KHz.

4 Conclusion

In this paper, we have demonstrated that a simple homodyne interferometer with a long coherence length laser can be used for *in vivo* PAI of biological tissue in quasinoncontact mode with constant high sensitivity. Using a zero-crossing trigger method, the interferometer is stabilized at its maximum sensitivity during imaging. The water layer on the sample surface provides a homogeneous surface for optical detection, and it plays a crucial role for the optical interferometry-based PAI. Future work will focus on improving the systematic sensitivity and decreasing the incident fluence of the excitation laser.

Compared with the acoustic detector-based PAI methods, such as using an ultrasound transducer or a Fabry–Perot polymer film ultrasound sensor, the present system can be easily miniaturized and has the potential to be developed into an endoscope system.

Disclosures

No conflicts of interest, financial or otherwise, are declared by the authors.

Acknowledgments

This research was supported in part by the National Natural Science Foundation of China (NSFC) (61275214 and 31170956), the Fundamental Research Funds for the Central Universities (N120223001), and the Hebei Provincial Natural Science Foundation of China (A2015501002 and H2015501133).

References

1. C. G. A. Hoelen et al., "Three-dimensional photoacoustic imaging of blood vessels in tissue," *Opt. Lett.* **23**(8), 648–650 (1998).
2. R. O. Esenaliev, A. A. Karabutov, and A. A. Oraevsky, "Sensitivity of laser opto-acoustic imaging in detection of small deeply embedded tumors," *IEEE J. Sel. Top. Quantum Electron.* **5**(4), 981–988 (1999).
3. L. V. Wang, "Multiscale photoacoustic microscopy and computed tomography," *Nat. Photonics* **3**(9), 503–509 (2009).
4. Y. Wang et al., "Photoacoustic imaging with deconvolution algorithm," *Phys. Med. Biol.* **49**(14), 3117–3124 (2004).
5. Y. Wang et al., "Fiber-laser-based photoacoustic microscopy and melanoma cell detection," *J. Biomed. Opt.* **16**(1), 011014 (2011).
6. H. F. Zhang et al., "Functional photoacoustic microscopy for high-resolution and noninvasive *in vivo* imaging," *Nat. Biotechnol.* **24**(24), 848–851 (2006).
7. C. Kim et al., "Deeply penetrating in vivo photoacoustic imaging using a clinical ultrasound array system," *Biomed. Opt. Exp.* **1**(1), 278–284 (2010).
8. K. Maslov et al., "Optical-resolution photoacoustic microscopy for in vivo imaging of single capillaries," *Opt. Lett.* **33**(9), 929–931 (2008).
9. S. Hu, K. Maslov, and L. V. Wang, "Second-generation optical-resolution photoacoustic microscopy with improved sensitivity and speed," *Opt. Lett.* **36**(7), 1134–1136 (2011).
10. E. Zhang, J. Laufer, and P. Beard, "Backward-mode multiwavelength photoacoustic scanner using a planar Fabry-Perot polymer film ultrasound sensor for high-resolution three-dimensional imaging of biological tissues," *Appl. Opt.* **47**(4), 561–577 (2008).
11. G. Paltauf et al., "Photoacoustic tomography using a Mach-Zehnder interferometer as an acoustic line detector," *Appl. Opt.* **46**(16), 3352–3358 (2007).
12. T. Berer et al., "Remote photoacoustic imaging on solid material using a two-wave mixing interferometer," *Opt. Lett.* **35**(24), 4151–4153 (2010).
13. S. A. Carp et al., "Optoacoustic imaging using interferometric measurement of surface displacement," *Appl. Phys. Lett.* **85**(23), 5772–5774 (2004).
14. G. Rousseau et al., "Non-contact biomedical photoacoustic and ultrasound imaging," *J. Biomed. Opt.* **17**(6), 061217 (2012).
15. A. Hochreiner et al., "Non-contact photoacoustic imaging using a fiber based interferometer with optical amplification," *Biomed. Opt. Exp.* **4**(11), 2322–2331 (2013).
16. S. J. Park et al., "Noncontact photoacoustic imaging based on all-fiber heterodyne interferometer," *Opt. Lett.* **39**(16), 4903–4906 (2014).
17. T. Berer et al., "Multimodal noncontact photoacoustic and optical coherence tomography imaging using wavelength-division multiplexing," *J. Biomed. Opt.* **20**(4), 046013 (2015).
18. Y. Wang, C. Li, and R. K. Wang, "Noncontact photoacoustic imaging achieved by using a low-coherence interferometer as the acoustic detector," *Opt. Lett.* **36**(20), 3975–3977 (2011).
19. Z. Chen et al., "All-optically integrated photo-acoustic microscopy and optical coherence tomography based on a single Michelson detector," *Opt. Lett.* **40**(12), 2838–2841 (2015).
20. J. Liu et al., "Rapid and noncontact photoacoustic tomography imaging system using an interferometer with high-speed phase modulation technique," *Rev. Sci. Instrum.* **86**(4), 22–31 (2015).
21. X. L. Deánben et al., "Non-contact optoacoustic imaging with focused air-coupled transducers," *Appl. Phys. Lett.* **107**(5), 051105 (2015).
22. J. Y. Kim et al., "Fast optical-resolution photoacoustic microscopy using a 2-axis water-proofing MEMS scanner," *Sci. Rep.* **5**, 7932 (2015).

Jiao Lu is a master's degree candidate at Northeastern University at Qinhuangdao. She received her BS degree in automation from Liaoning Institute of Science and Technology in 2012. Her current research interests include photoacoustic imaging and optical coherence tomography.

Zhenhe Ma is an associate professor of biomedical engineering at Northeastern University at Qinhuangdao. He received his PhD degree from Tianjin University in 2007. His research interests are in photoacoustic imaging and optical coherence tomography.

Yi Wang is a professor of biomedical engineering at Northeastern University at Qinhuangdao. He received his PhD degree from Xi'an Jiaotong University in 2002. His current research interests include photoacoustic imaging and optical coherence tomography.

Biographies for the other authors are not available.